

Article

Cracking Behavior and High-Temperature Thermoplastic Analysis of 09CrCuSb Steel Billets

Zhixian Peng ^{1,*}, Tao Mei ¹, Jian Zheng ², Yuan Yuan ² and Liwang Wang ³

¹ State Key Laboratory of Refractory Materials and Metallurgy, Wuhan University of Science and Technology, Wuhan 430081, China

² Hunan Hualing Xiangtan Iron and Steel Co., Ltd., Xiangtan 411101, China

³ Zhejiang Jincheng New Material Co., Ltd., Changxing 313100, China; wanglw5133@163.com

* Correspondence: pengzhixian@wust.edu.cn

Abstract: This paper characterizes the surface crack morphology and elements of 09CrCuSb steel continuous casting slabs and studies the high-temperature thermo-plasticity of continuous casting slabs using a Gleeble 3500 thermal simulator. Combining the macro/micro fracture morphology and microstructure characteristics, the formation rules of slab cracks are discussed. The research results show that the increase in Ae3 temperature caused by changes in alloy elements results in the precipitation of a thin, film-like coexisting ferrite along the grain boundaries at a certain temperature, as well as the element segregation behavior of low-melting-point alloy elements at the original austenite grain boundaries, which are the main factors inducing cracks in 09CrCuSb steel continuous casting billets. The plasticity of 09CrCuSb steel at high temperatures is poor at 800~900 °C. In continuous casting process control, it is necessary to try to avoid long-term stay of the billet at this temperature range.

Keywords: 09CrCuSb; high-temperature thermoplastic; continuous casting billet cracking; boiler steel



Citation: Peng, Z.; Mei, T.; Zheng, J.; Yuan, Y.; Wang, L. Cracking Behavior and High-Temperature Thermoplastic Analysis of 09CrCuSb Steel Billets. *Metals* **2023**, *13*, 1058. <https://doi.org/10.3390/met13061058>

Academic Editor: Francesco Iacoviello

Received: 27 April 2023

Revised: 28 May 2023

Accepted: 30 May 2023

Published: 31 May 2023



Copyright: © 2023 by the authors. Licensee MDPI, Basel, Switzerland. This article is an open access article distributed under the terms and conditions of the Creative Commons Attribution (CC BY) license (<https://creativecommons.org/licenses/by/4.0/>).

1. Introduction

09CrCuSb steel, also known as ND steel, is widely used in equipment and devices that require resistance to low-temperature dew point corrosion of sulfur-containing flue gas due to its excellent performance in this area [1,2]. According to the new national energy industry standard “Technical Requirements for Steel Tubes for Boilers and Heat Exchangers NB/T47019-2021” implemented on 1 July 2021 in China [3], significant changes have been made to the composition of 09CrCuSb steel, particularly with a substantial increase in elements such as Cu, Sb, Sn, Mo, and W. The significance of the above elements’ addition lies in the improvement of dew point corrosion resistance of sulfur-containing flue gas [4,5]. However, this has resulted in severe surface cracks in the continuous casting process, which not only increases the cost of repairs but also affects the quality of subsequent rolled products [6–9].

Many scholars have conducted research on the cracking of continuous casting billets of 09CrCuSb steel. For example, from the aspect of the cast process, Hu et al. [10] analyzed the crack morphology at the corners of 09CrCuSb steel and combined it with finite element simulation to analyze the temperature distribution in the second cooling zone during casting, determining that the cracks occurred mainly in the secondary water cooling zone during the casting process. Based on a 2D heat transfer model’s real-time temperature field analysis for the entire slab section and process, Chen et al. [11] summarized that reducing or increasing the water flux in secondary cooling zones by over 20% and 80%, respectively, can maintain good thermoplastic properties in the straightening zone and can lower the risk of corner transverse crack formation. Furthermore, it should be noted that due to the high content of easy segregation elements at the grain boundaries, such as Cu, Sb, Sn, etc., in the alloy composition of 09CrCuSb steel, the problem of interface weakening caused by

grain boundary segregation at high temperatures should also be taken seriously [12,13]. Chen et al. [6] studied the mechanism of surface crack formation in 09CrCuSb steel and found that surface crack defects were caused by slag oxidation and Cu element enrichment. In a similar study, Zhou et al. [14] found that Cu is hard to move from the grain boundary to the steel matrix in continuous casting due to its solubility being high and the diffusion coefficient being low in Fe. This leads to weakened grain boundaries that can cause cracks when the billet is bent or straightened [15,16]. Lu [17] analyzed the elements near the cracks of 09CrCuSb steel castings and found that there was a significant correlation between the presence of Cu and Sb precipitation phases and crack initiation. Huang [18] found that when the segregation of residual elements Sn and Sb on the grain boundaries was high, the thermal plasticity of the material was poor. Therefore, under the new national standard composition requirements, the research on the cracking of continuous casting billets of 09CrCuSb steel should further explore the distribution of crystal boundary elements and the process parameters, understand the micro-mechanism of billet cracking, and propose corresponding solutions.

This article focuses on the continuous casting billets of 09CrCuSb steel and analyzes and discusses the causes of cracking from the perspectives of high-temperature phase transformation and grain boundary segregation of elements. The recommendations for improving the process are also included based on thermal simulation, optical microscopy (OM), electron probe microanalysis (EPMA), and scanning electron microscopy + energy-dispersive X-ray spectroscopy (SEM + EDS).

2. Materials and Experimental Procedure

This experiment focuses on the preparation of 09CrCuSb steel continuous casting billets using the composition specified in the NB/T47019-2021 [3] national standard. The chemical composition is shown in Table 1. The continuous casting process has a casting cross-sectional size of 280 mm × 280 mm, a maximum overheat temperature of 30 °C in the tundish, a pulling speed of 0.95 m/min, and a measured temperature at the billet surface of 998 °C and at the corners of 916 °C during casting. After passing through the straightening machine, the measured temperatures at the billet surface and corners were 910 °C and 805 °C, respectively. After the casting process, the red billet showed no visible defects such as cracks or scratches, but macroscopic cracks were present on the surface of the continuous casting billet.

Table 1. Composition analysis of experimental steels (wt. %).

09CrCuSb	C%	P%	S%	Cu%	Cr%
	0.06	0.009	0.003	0.45	0.95
	Sn%	Sb%	W%	Ni%	Ceq%
	0.13	0.192	0.183	0.24	0.42

To further investigate the thermal deformation behavior of materials under high temperature conditions, samples were taken along the direction of the continuous casting billet near the surface of the casting billet and subjected to hot tensile tests using a Gleeble 3500 thermal simulator. The hot tensile test used a cylindrical sample with a diameter of 10 mm. First, the sample was heated at a rate of 10 °C/s to 1320 °C and maintained for 4 min, and then cooled to the target temperature (600~1300 °C) at a cooling rate of 10 °C/s and maintained for 2 min. After that, the sample was stretched at a strain rate of 10⁻³ s⁻¹. When the sample fractured, an inert gas was used to rapidly cool the sample. A Zeiss Axio Scope A1 metallographic microscope, KEYENCE VHX5000 digital microscope, and Thermo-Fisher Apreo-S HiVac field emission scanning electron microscope were used to observe the cracks in the casting billet, the fracture surface and longitudinal section of the samples, and the distribution of crack elements. Additionally, the Shimadzu 8050 G electron probe microanalysis was used to improve the recognition of the elemental influence on the initiation of cracks in billets.

3. Results

3.1. Crack Morphology and Elemental Analysis of 09CrCuSb Continuous Casting Billet

Figure 1 depicts the cross-sectional morphology of cracks observed within continuous casting billets, characterized by two specific regions. In Figure 1a, the presence of a main crack extending along the plate-like ferrites toward the surface of the billets evidences its significance in the initial stages of crack formation, alongside cracks originating from inside the ferrite. In contrast, Figure 1b demonstrates a crack with apparent secondary cracks following the ferrite direction. The figure shows that the depth of the billet cracks exceeds 700 μm at the deepest point, and the austenite structure around the cracks is relatively coarse. Thin-film pearlite is distributed in a net-like manner along the original austenite structure, while the cracks exhibit characteristics of extension along the pearlite thin film. Inside the original austenite grains, the structure is characterized by small, interlocking acicular pearlite. Further analysis was conducted on the elements around the crack area in Figure 1b using energy spectrum analysis under a scanning electron microscope, as shown in Figure 2. It can be clearly observed that the elements Cr, Cu, and Sb are enriched along the interior of the crack.

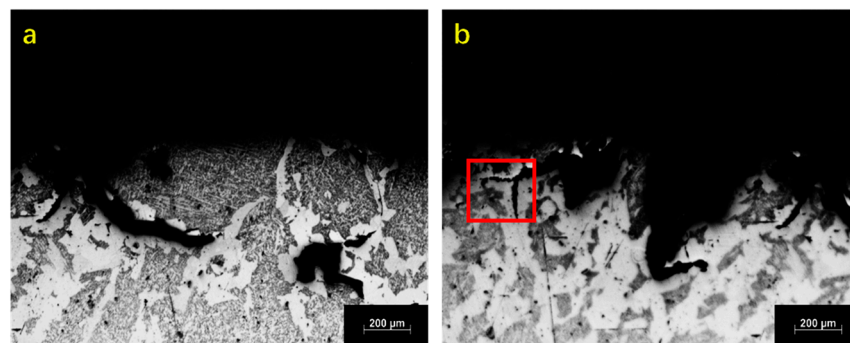


Figure 1. Microscopic morphology of cracks in continuous casting billets, regions 1 (a) and 2 (b).

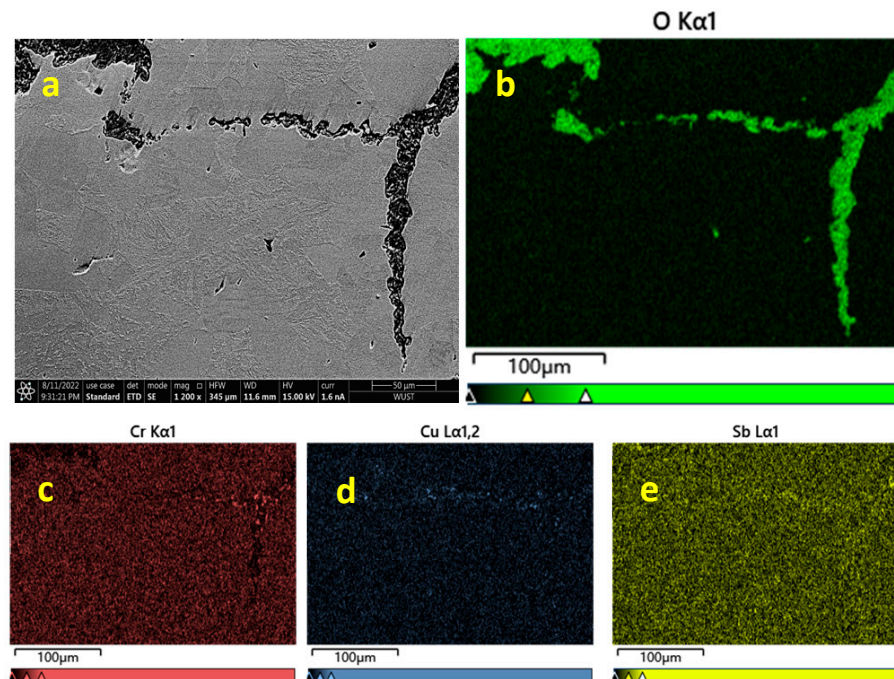


Figure 2. SEM morphology (a) and energy spectrum maps (b–e) of local surface cracks on continuous casting billets.

3.2. High-Temperature Thermo-Plasticity of 09CrCuSb Steel

Figure 3 shows the tensile properties and high-temperature strength and section shrinkage rate at different temperatures. The calculation formula for the section shrinkage rate of the tensile fracture is $A = (D_0^2 - D_i^2)/D_i^2$, where D_0 is the original diameter of the sample, and D_i is the diameter of the tensile fracture at different temperatures. From the trend of strength change, as the insulation temperature increases, the overall tensile strength of the material tends to decrease, which is similar to the results reported in [19]. For high-temperature plasticity of the material, the section shrinkage rate of the tensile fracture gradually increases with the temperature rising in the range of 600–750 °C, and the section shrinkage rate is greater than 40% in this temperature range. Figure 4a–c show obvious necking features of the fracture, indicating that the plasticity of the material is better in this temperature range [20]. Combined with the fracture morphology under SEM in Figure 5a–c, the fracture presents obvious ductile dimples at 600 °C, and some inclusions can be observed at the bottom of some dimples. As the temperature further increases, the depth of the dimples becomes shallower and the internal pattern becomes fragmented, and there are only a few ductile dimple features, indicating that the plasticity of the material decreases with the temperature increase.

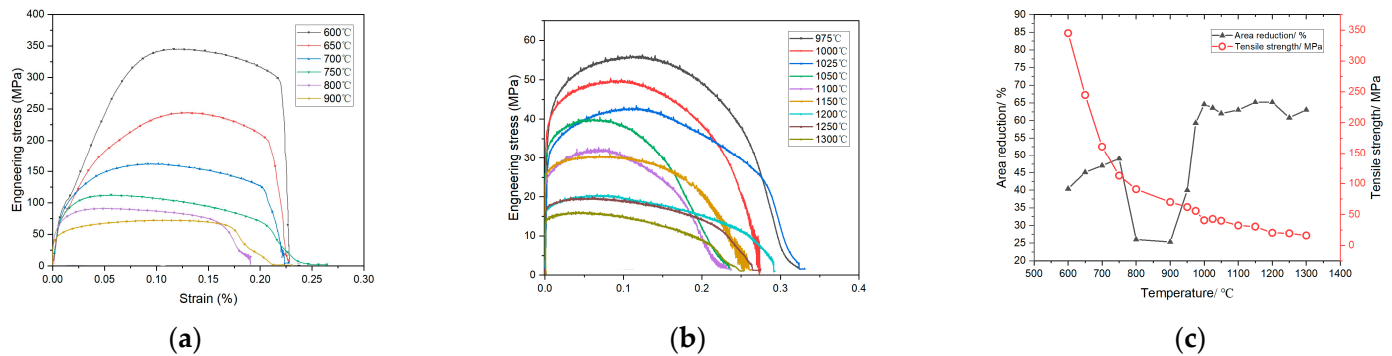


Figure 3. Thermal tensile stress–strain curves (a,b) at different temperatures, changes in thermal tensile strength and reduction of area (c).

When the hot tensile test is conducted in the temperature range of 800–900 °C, the section shrinkage rates at the two temperatures are 26.0% and 25.4%, respectively, and the section shrinkage rate of the samples decreases significantly, indicating that the plasticity of the material is significantly reduced. From the macroscopic morphology of the fracture (such as Figure 4d–f), when the tensile temperature is 800 °C, the hot tensile fracture has a flat step surface but no obvious necking features, and the section shrinkage rate of the samples is lower and the plasticity inferior. Further observation of the fracture morphology under scanning electron microscopy (Figure 5d) shows typical brittle cleavage features on the fracture. Unlike the results obtained by Hu et al. [10,19], the plasticity of the 09CrCuSb steel under the new component system is in a trough zone between 800 and 900 °C, which is the third brittle temperature range of the 09CrCuSb steel.

When the hot tensile temperature is above 1000 °C, the section shrinkage rate increases significantly to over 60%, the macroscopic fracture shows necking features (such as Figure 4f–h), and the section is relatively flat. The SEM morphology of the fracture shows shallower ductile dimples, as shown in Figure 5c. As the temperature further increases, there are many high-temperature molten beads on the fracture that are difficult to further analyze, but the necking features become more obvious, as shown in Figure 4d–i. When the temperature is above 1100 °C, the section shrinkage rate further increases and the necking features become more obvious, showing good high-temperature plasticity.

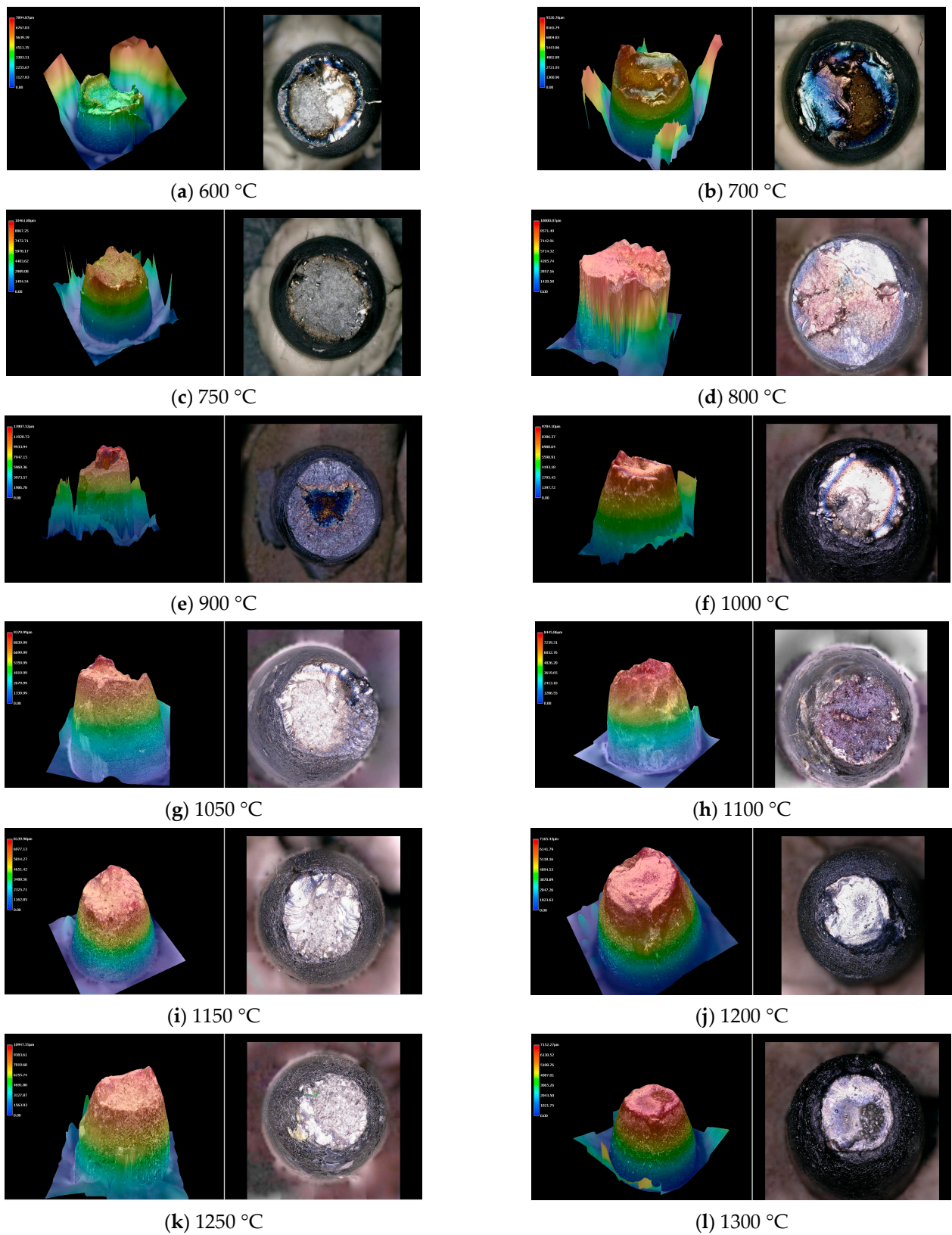


Figure 4. Macromorphology of hot stretching fractures at different temperatures.

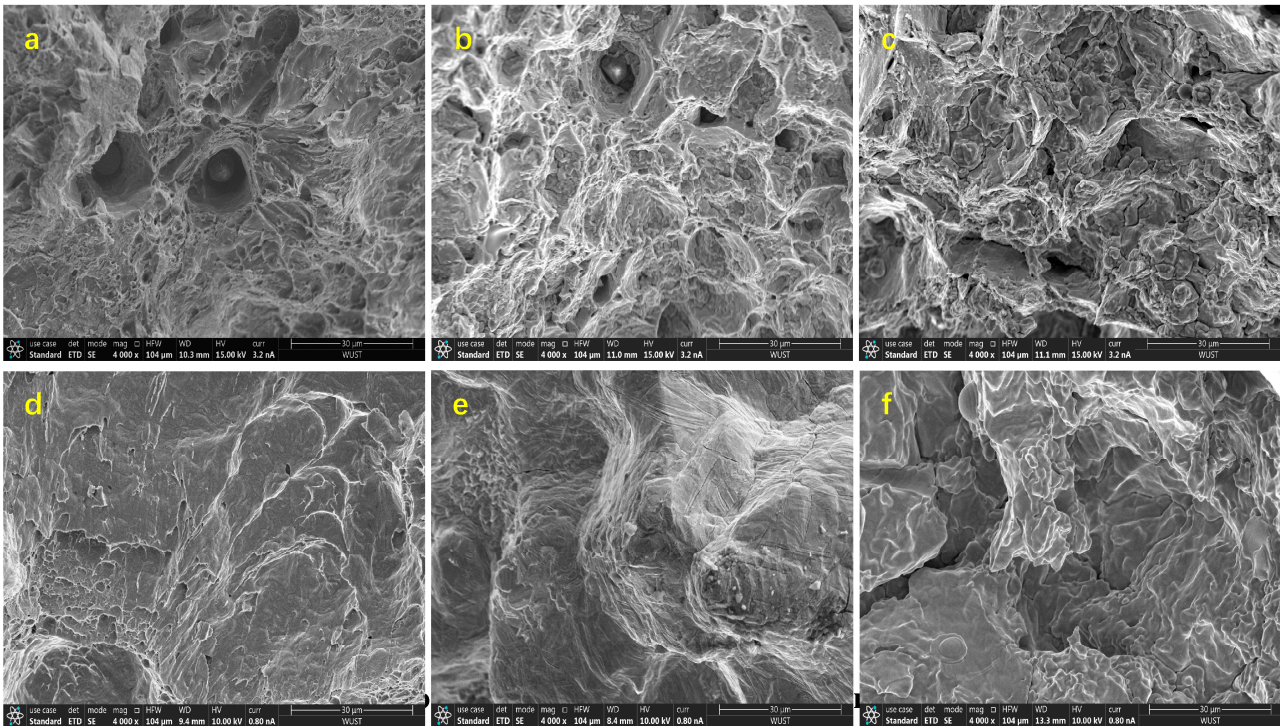


Figure 5. SEM morphology of hot tensile fracture at different temperatures: 600 °C (a), 700 °C (b), 750 °C (c), 800 °C (d), 900 °C (e), 1000 °C (f).

When the stress on the material is between the yield point strength and the tensile strength, the specimen will undergo uniform plastic deformation. At this time, a small deformation amount will cause stress concentration, causing the stress on the material to quickly increase to the ultimate strength and cause fracture. By calculating the plastic modulus of the deformation stage, it can be used as an evaluation index of material plastic strengthening. For high-temperature tensile cast specimens, the larger the plastic modulus, the worse the plasticity, that is, the more likely it is to break at a certain temperature [21]. Based on the Hollomon formula, the plastic modulus of the material satisfies the following relationship [22,23].

$$\sigma = H\varepsilon^n \quad (1)$$

Among them, ε is the true strain of the material, σ is the true stress, and H is the plastic modulus of the material. Since the strain rate in this experiment can be considered constant, taking the logarithm of Equation (1) on both sides and differentiating it, by calculating the instantaneous slope value of the true stress–strain curve in the logarithmic coordinate system, we can further obtain the hardening index n of the material [22,23]:

$$n = \frac{d \lg \sigma}{d \lg \varepsilon} \quad (2)$$

The relationship between the plastic modulus H and the temperature of the material, as shown in Figure 6, can be obtained by processing the true stress–strain curves under different temperatures. The n values in the fitting process are distributed in the range of 0.05 to 0.5, indicating a good fitting result [23]. From the variation of the plastic modulus obtained by the fitting with the temperature, the overall trend of the plastic modulus is decreasing. At temperatures of 600–750 °C, the plastic modulus value is relatively large but the change relatively flat, with the highest value appearing at 700 °C. When the temperature is above 750 °C, the plastic modulus value rapidly decreases, and the change slows down after 900 °C. The highest value appears again at 975 °C, and finally slowly decreases with the increase of temperature. From the results of the high-temperature plastic modulus, it

can be seen that the plasticity of 09CrCuSb steel is poor around 700 °C, so it should be avoided as much as possible to have significant deformation at 700 °C during hot rolling. When the temperature is above 800 °C, the plastic deformation ability of 09CrCuSb steel also decreases significantly, so in the continuous casting process, the two-water control process should also avoid the billet staying at a temperature of 800–975 °C for a long time [21].

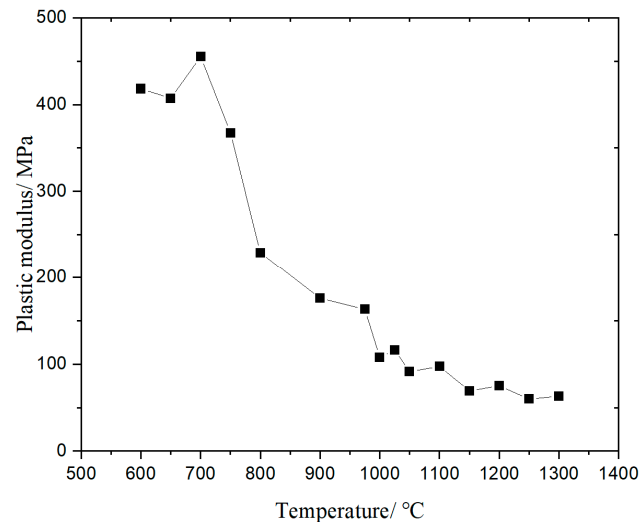


Figure 6. Change of plastic modulus (dotted line) of 09CrCuSb steel with temperature.

3.3. Microstructure Deviation and Elements Segregation near Cracks in 09CrCuSb Steel during the High-Temperature Tensile Process

The organizational characteristics of the longitudinal section of the fracture after hot tensile testing of 09CrCuSb steel at different temperatures are shown in Figure 7a–i. From Figure 7a, it can be seen that when the tensile temperature is 600 °C, the structure near the fracture is composed mainly of ferrite and pearlite. Observing the secondary cracks near the fracture, it can be seen that the cracks extend along the original austenite grains. Comparing Figure 7a–c, it can be seen that as the tensile temperature increases, both the ferrite and pearlite structures undergo obvious coarsening, which is consistent with the grain isothermal growth model proposed by E. Anelli et al. [24]. When the temperature reaches 800 °C, as shown in Figure 7d, the fracture and secondary cracks extend mainly along the original austenite grain boundary, and there is an obvious film-like proeutectoid ferrite structure near the original austenite grain boundary, which is consistent with the observed organizational characteristics near the casting crack, and the structure near the center of the austenite grain is displayed mainly as granular bainite and acicular ferrite. When the hot tensile temperature is 900 °C, the longitudinal section of the fracture and secondary cracks also show the characteristic of extension along the proeutectoid ferrite, and the structure near the center is mainly acicular ferrite, as shown in Figure 7e. Comparing Figure 7d–f, as the temperature increases within 800–1000 °C, the grain size of the ferrite structure around the original austenite grain boundary tends to increase, and the thickness of the film-like proeutectoid ferrite at the austenite grain boundary also gradually increases. When the hot tensile temperature is greater than 1050 °C (as in Figure 7g–i), the film-like proeutectoid ferrite on the longitudinal section of the fracture disappears, and the internal organization near the fracture is composed mainly of bainite. When the hot tensile temperature is 1300 °C, the fracture surface becomes flat and displays the characteristics of Type I high-temperature brittle fracture.

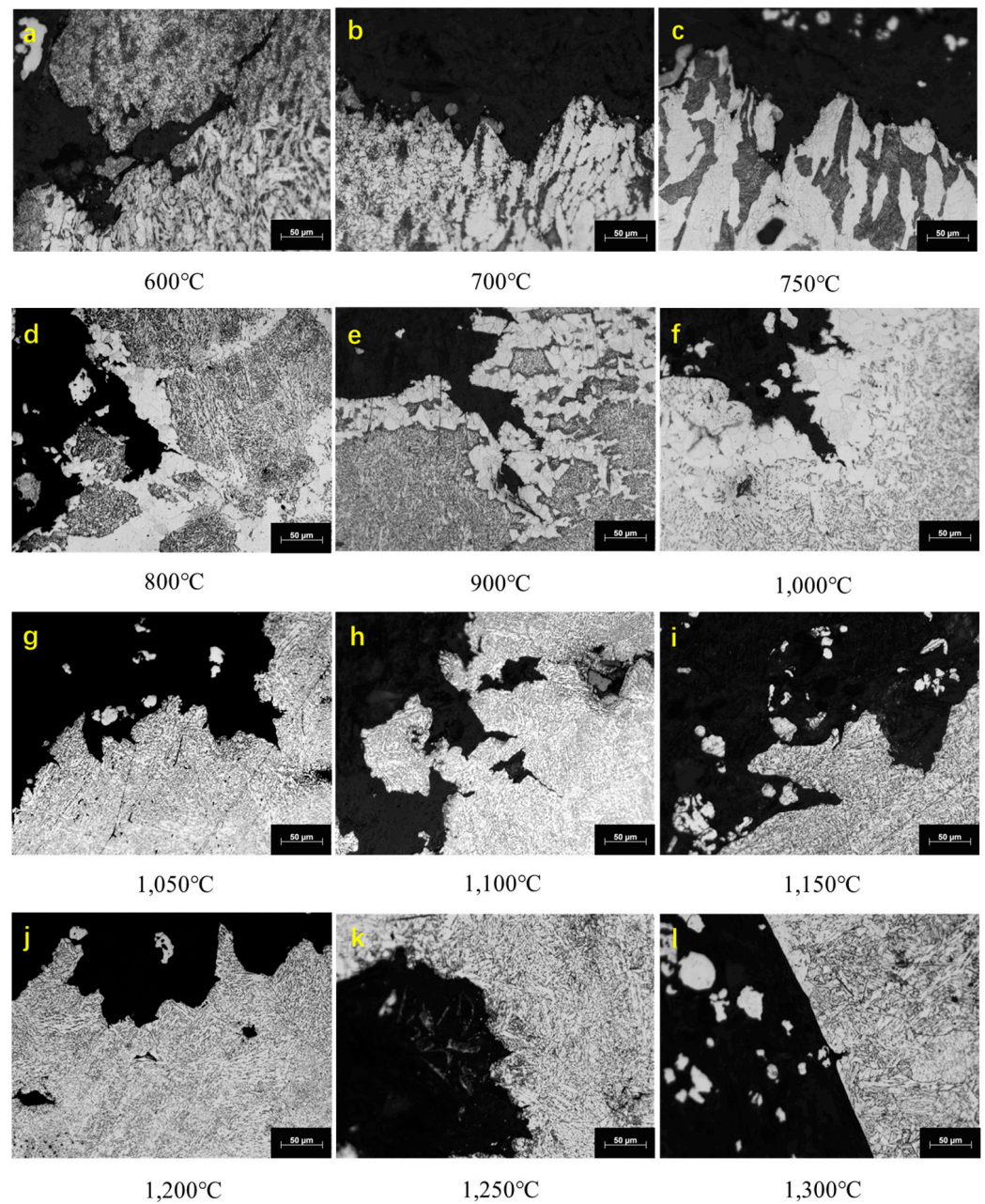


Figure 7. Metallographic structure of hot stretching fracture section at different temperatures.

The EPMA analysis of the crack near the tested area under 800 °C thermal tensile conditions are depicted in Figure 8. The elemental map indicates a higher content of carbon in the bainites and at the grain boundaries of proeutectoid ferrites. Furthermore, Cu exhibits clear segregation at the ferrite triple junctions as red circled in Figure 8, whereas there is no noticeable segregation behavior for Cr. Zhou et al. [14] have similarly concluded that elevated temperatures during continuous casting exhibit a high level of Cu solubility, with a thermal threshold exceeding 900 °C. Yet, the low diffusion coefficient of Cu within Fe presents a substantial obstacle for the material to infiltrate the steel matrix, particularly where the grain boundary has experienced Cu buildup.

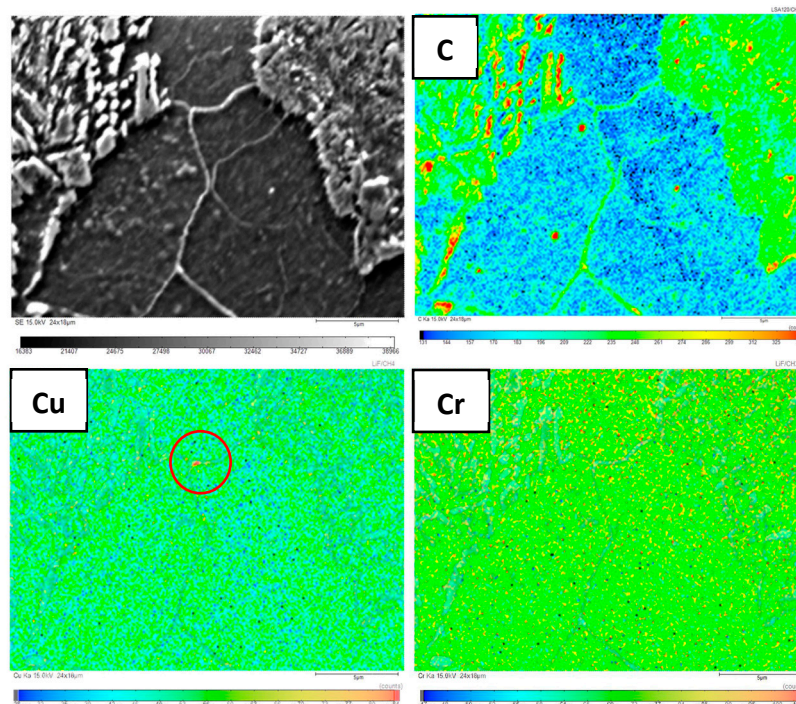


Figure 8. EPMA analysis on the crack face adjacent area after fracture under 800 °C.

4. Discussion

From Figures 1 and 7, it can be observed that there are obvious film-like proeutectoid ferrite grain boundaries near the crack and the 800–1000 °C tensile fracture surface of the billet, and secondary cracks also mainly occur and propagate in the proeutectoid ferrite grain boundaries distributed along the austenite grain boundaries. According to the classification of allotriomorphic ferrite by Yang et al. [25], both sides of the allotriomorphic ferrite near the crack in the billet have uneven and unclear boundary contours and belong to the GF-II type allotriomorphic ferrite, which is formed by the nucleation of original austenite grain boundaries and growth inward. Li et al. [26] pointed out that one of the essential influences of austenite deformation on the nucleation and incubation period of proeutectoid ferrite is that the deformation intensifies the disorder of the atomic arrangement on the austenite grain boundary, causing the increase of grain boundary energy and promoting the nucleation of proeutectoid ferrite. Thus, during the process of casting, the high temperature provides the formation condition of austenite, and the casting forming provides the intensified disorder of the atomic arrangement. The plate-like proeutectoid ferrites is easy to nucleate along the austenite boundaries.

It should be noted that compared with the old version of the energy standard NB/T47019-2011 [27], the newly issued NB/T47019-2021 standard has increased the content of proeutectoid-forming elements such as Cr, Mo, Si, Nb, Al, and Ti [28,29], which is represented by the Ae3 temperature increasing from 855 °C to 880 °C on the phase diagram, as calculated by the Thermal-Calc software in Figure 9. Ae3 temperature represents the beginning temperature of the thermodynamic austenite–ferrite transformation [30–33]. It can be seen that the increase of alloy elements means that the transformation time of proeutectoid ferrite during the cooling process is advanced due to the increase of Ae3 temperature [33,34]. It also means that during the cooling process, the formation of ferrite will happen before it would in steel [35]. Therefore, when the slab enters the straightening machine during continuous casting, the surface temperature due to the effect of reheating should return to above 800 °C. The expansion of the two-phase region leads to the extension of the insulation time of the billet in the two-phase region, and proeutectoid ferrite precipitation is also promoted when the grain boundary satisfies certain thermodynamic conditions. Given the crucial role of proeutectoid ferrite formation, it is important to give due consideration to carbon content.

process should be adjusted to avoid the billet staying at a temperature range of 800–900 °C for a long time.

5. Conclusions

(1) The cracking observed on the surface of 09CrCuSb steel castings can be attributed to two primary factors. First, the modification in alloy composition results in an increase in the Ae3 temperature (from 855 °C to 880 °C), leading to the precipitation of a thin, film-like coexisting ferrite along the grain boundaries. Second, alloying elements have a higher propensity to experience non-equilibrium segregation at grain boundaries, which weakens the austenite grain boundary strength. This feature eventually leads to surface embrittlement and the formation of cracks on the castings.

(2) The 09CrCuSb steel has poor plasticity at 700 °C, making it unsuitable for hot rolling in the pipe-making process. Between 800 and 900 °C, the steel enters the third brittle temperature range. To prevent damage, castings need to avoid staying in this temperature range for too long during the two-phase cooling process of continuous casting.

(3) The stress–strain curve of 09CrCuSb steel at various test temperatures shows a gradual decrease in its plastic modulus with increasing temperature. The material exhibits good plastic deformation between 600 and 650 °C. When the temperature exceeds 1000 °C, the plastic modulus is low (<80 MPa), indicating that the castings can withstand large uniform plastic deformation at high temperatures.

Author Contributions: Conceptualization, Z.P.; methodology, T.M. and Z.P.; validation, Z.P., T.M. and Y.Y.; formal analysis, Z.P.; investigation, Z.P., Y.Y. and J.Z.; resources, J.Z. and Y.Y.; data curation, J.Z. and Y.Y.; writing—original draft preparation, Z.P. and T.M.; writing—review and editing, J.Z.; supervision, L.W.; project administration, J.Z. and L.W.; funding acquisition, Z.P. All authors have read and agreed to the published version of the manuscript.

Funding: This work is funded by National Natural Science Foundations of China (52201084).

Institutional Review Board Statement: Not applicable.

Informed Consent Statement: Informed consent was obtained from all subjects involved in the study.

Data Availability Statement: Because data is unavailable due to privacy, where no new data were created.

Acknowledgments: Postdoctoral Station of Metallurgical Engineering of Wuhan University of Science and Technology, Postdoctoral Workstation of Zhejiang Jincheng New Material Co., Ltd. This work also thanks the Analysis and Testing Centre of Wuhan University of Science and Technology.

Conflicts of Interest: The authors (Zhixian Peng, Tao Mei, Jian Zheng, Yuan Yuan, Liwang Wang) declare that we have no financial and personal relationships with other people or organizations that could inappropriately have influenced our work, there is no professional or other personal interest of any nature or kind in any product, service and/or company that could be construed as influencing the position presented in or review of this manuscript. The authors declare no conflict of interest.

References

1. Cai, H. Application of 09CrCuSb Steel in Boiler Manufacturing. *Ind. Boil.* **2005**, *5*, 22–25.
2. Ling, L.; Xu, X.; Fu, H. Welding Practice of 09CrCuSb Sulfuric Acid Dew Point Corrosion Resistant Steel. *Medium Nitrogen Fertil.* **2011**, *2*.
3. NB/T47019-2021; Technical Conditions for Ordering Pipes for Boilers and Heat Exchangers. National Energy Administration of China: Beijing, China, 2021.
4. Zuo, W.; Zhang, X.; Li, Y. Review of flue gas acid dew-point and related low temperature corrosion. *J. Energy Inst.* **2020**, *93*, 1666–1677. [[CrossRef](#)]
5. Zeng, Y.; Li, K.; Hughes, R.; Luo, J.-L. Corrosion mechanisms and materials selection for the construction of flue gas component in advanced heat and power systems. *Ind. Eng. Chem. Res.* **2017**, *56*, 14141–14154. [[CrossRef](#)]
6. Chen, Z.; Wang, Q.; Cai, Y.; Wang, Z. Analysis on the Formation Mechanism of Surface Cracks on 09CrCuSb Billets. *Mod. Transp. Metall. Mater.* **2021**, *1*, 83–87.
7. Yu, H.; Wang, Y.; Zhang, J.; Yang, S.; Liu, X. Review on the Causes of Surface Cracks in Continuous Casting Billets and Their Evolutionary Behavior during Rolling Process. *Forg. Stamp. Technol.* **2010**, *2*, 1–5.

8. Ito, K.; Tanaka, Y.; Sawada, H. Application of Grain Boundary Segregation Prediction Using a Nano-Polycrystalline Grain Boundary Model to Transition Metal Solute Elements: Prediction of Grain Boundary Segregation of Mn and Cr in bcc-Fe Polycrystals. *Mater. Trans.* **2022**, *63*, 269–277. [[CrossRef](#)]
9. Han, J.P.; Li, Y.; Jiang, Z.H.; Yang, Y.C.; Wang, X.X.; Wang, L.; Li, K.T. Summary of the Function of Sn in Iron and Steel. In *Advanced Materials Research*; Trans Tech Publications Ltd.: Bäch, Switzerland, 2013; pp. 406–411.
10. Hu, H.; Zhu, L.; Sun, L.; Zhou, J. Mechanism and Preventive Measures of Corner Cracks in 09CrCuSb Steel Continuous Casting Billets. *Shanghai Met.* **2020**, *42*, 7.
11. Chen, Y.; Ji, C.; Zhu, M. Prediction Model of the Proeutectoid Ferrite Growth of a Continuous Casting Slab. *Metall. Mater. Trans.* **2023**, *54*, 1101–1115. [[CrossRef](#)]
12. Wei, F.; Cheng, B.; Chew, L.T.; Lee, J.J.; Cheong, K.H.; Wu, J.; Zhu, Q.; Tan, C.C. Grain distribution characteristics and effect of diverse size distribution on the Hall–Petch relationship for additively manufactured metal alloys. *J. Mater. Res. Technol.* **2022**, *20*, 4130–4136. [[CrossRef](#)]
13. Cao, J.; Dong, J.; Saglik, K.; Zhang, D.; Solco, S.F.D.; You, I.J.W.J.; Liu, H.; Zhu, Q.; Xu, J.; Wu, J. Non-equilibrium strategy for enhancing thermoelectric properties and improving stability of AgSbTe₂. *Nano Energy* **2023**, *107*, 108118. [[CrossRef](#)]
14. Zhou, J.; Zhu, L.; Sun, L.; Wang, B.; Xiao, P. Analysis of the Formation Mechanism of Surface Cracks of Continuous Casting Slabs Caused by Mold Wear. *Processes* **2022**, *10*, 797. [[CrossRef](#)]
15. Al-Asad, M.; Alam, M.N.; Tunç, C.; Sarker, M. Heat Transport Exploration of Free Convection Flow inside Enclosure Having Vertical Wavy Walls. *J. Appl. Comput. Mech.* **2021**, *7*, 520–527.
16. Akinshilo, A.; Davodi, A.; Reza zadeh, H.; Sobamowo, G.; Tunç, C. Heat Transfer and Flow of Mhd Micropolar nanofluid through the Porous Walls, Magnetic Fields and Thermal Radiaton. *Palest. J. Math.* **2022**, *11*, 604–616.
17. Lu, T. *Analysis on the Causes of Surface Cracks in 09CrCuSb Billets and Improvement Measures*; Anhui University of Technology: Ma'anshan, China, 2016.
18. Huang, X. *The Effect of Grain Boundary Segregation of Residual Elements As, Sn, Sb on the Thermoplasticity of Continuous Casting Steel*; Wuhan University of Science and Technology: Wuhan, China, 2006.
19. Hu, H.; Zhu, L.; Sun, L.; Zhou, J. High Temperature Mechanical Properties of 09CrCuSb Steel Continuous Casting Billets. *Iron Steel Vanadium Titan.* **2020**, *41*, 132–136.
20. Mintz, B. The influence of composition on the hot ductility of steels and to the problem of transverse cracking. *ISIJ Int.* **1999**, *39*, 833–855. [[CrossRef](#)]
21. Chen, D.; Huang, L.; Wang, Y.; Wen, L.; Feng, K.; Liu, Q.; Han, Z. Experimental Study on High Temperature Plastic Modulus of Q345 Steel. In Proceedings of the 2006 National Metallurgical Physical Chemistry Academic Conference of China, Jinan, China, 29–30 December 2006.
22. Zener, C.; Hollomon, J.H. Effect of strain rate upon plastic flow of steel. *J. Appl. Phys.* **1944**, *15*, 22–32. [[CrossRef](#)]
23. Meyers, M.A.; Chawla, K.K. *Mechanical Behavior of Materials*; Cambridge University Press: Cambridge, UK, 2008.
24. Anelli, E. Application of mathematical modelling to hot rolling and controlled cooling of wire rods and bars. *ISIJ Int.* **1992**, *32*, 440–449. [[CrossRef](#)]
25. Yang, Z.; Wang, K.; Sun, X.; Da, G. Morphology of grain boundary ferrite and grain boundary cracks in niobium titanium microalloyed steel billets. *Iron Steel* **2018**, *53*, 10.
26. Li, J.; Sun, F. The Effect of Austenitic Deformation on the Incubation Period of Isothermal Formation of Pre eutectoid Ferrite. *Acta Metall. Sin.* **1990**, *4*, 161–164.
27. *NB/T47019-2011*; Technical Conditions for Ordering Pipes for Boilers and Heat Exchangers. National Energy Administration of China: Beijing, China, 2011.
28. Liu, M.; Li, Y.; Cui, Z.; Yang, Q. High ductility of spray formed low density TRIP steel with the improvement of δ -ferrite matrix. *Mater. Charact.* **2019**, *156*, 109828. [[CrossRef](#)]
29. Shao, Y.; Liu, C.; Yan, Z.; Li, H.; Liu, Y. Formation mechanism and control methods of acicular ferrite in HSLA steels: A review. *J. Mater. Sci. Technol.* **2018**, *34*, 737–744. [[CrossRef](#)]
30. Equihua-Guillén, F.; Salinas-Rodriguez, A. Role of the austenite-ferrite transformation start temperature on the high-temperature ductility of electrical steels. *J. Mater. Eng. Perform.* **2011**, *20*, 102–107. [[CrossRef](#)]
31. Ghosh, C.; Aranas, C., Jr.; Jonas, J.J. Dynamic transformation of deformed austenite at temperatures above the Ae₃. *Prog. Mater. Sci.* **2016**, *82*, 151–233. [[CrossRef](#)]
32. Toloui, M.; Militzer, M. Phase field modeling of the simultaneous formation of bainite and ferrite in TRIP steel. *Acta Mater.* **2018**, *144*, 786–800. [[CrossRef](#)]
33. Maubane, D.R.N.; Mostert, R.J.; Banks, K.M. Re-Austenitisation of Thin Ferrite Films in C–Mn Steels during Thermal Rebound at Continuously Cast Slab Corner Surfaces. *Metals* **2022**, *12*, 2155. [[CrossRef](#)]
34. Aaronson, H.; Reynolds, W.; Purdy, G. Coupled-solute drag effects on ferrite formation in Fe–CX systems. *Metall. Mater. Trans. A* **2004**, *35*, 1187–1210. [[CrossRef](#)]
35. Kwok, T.; Dye, D. A review of the processing, microstructure and property relationships in medium Mn steels. *Int. Mater. Rev.* **2023**, 1–37. [[CrossRef](#)]
36. Yin, J.; Hillert, M.; Borgenstam, A. Morphology of proeutectoid ferrite. *Metall. Mater. Trans. A* **2017**, *48*, 1425–1443. [[CrossRef](#)]

37. Li, F.; Tian, J.; Li, H.; Deineko, L.; Jiang, Z. Simultaneously Enhancing Strength, Ductility and Corrosion Resistance of a Martensitic Stainless Steel via Substituting Carbon by Nitrogen. *Acta Metall. Sin. (Engl. Lett.)* **2023**, *36*, 705–716. [[CrossRef](#)]
38. Liu, F.; Kang, C.; Qian, R.; Jiang, Z.; Geng, X.; Li, H. Effect of Tempering Temperature on Microstructure and Properties of a New Type of Nitrogen—Containing Hot-Work Die Steel 3Cr7Mo2NiSiVN. *Steel Res. Int.* **2022**, *93*, 2200013. [[CrossRef](#)]
39. Yang, Y.; Jia, X.; Ma, Y.; Wang, P.; Zhu, F.; Yang, H.; Wang, C.; Wang, S. Effect of Nb on microstructure and mechanical properties between base metal and high heat input coarse-grain HAZ in a Ti-deoxidized low carbon high strength steel. *J. Mater. Res. Technol.* **2022**, *18*, 2399–2412. [[CrossRef](#)]
40. Anthony, T.R. Solute segregation in vacancy gradients generated by sintering and temperature changes. *Acta Metall.* **1969**, *17*, 603–609. [[CrossRef](#)]
41. Yang, S.; Ma, J.; Chen, C.; Zhang, C.; Ren, J.; Jiang, Z.; Fan, G.; Han, P. Effects of B and Ce Grain Boundary Segregation on Precipitates in Super Austenitic Stainless Steel. *Metals* **2023**, *13*, 326. [[CrossRef](#)]
42. Xu, T. Non-equilibrium grain-boundary segregation kinetics. *J. Mater. Sci.* **1987**, *22*, 337–345. [[CrossRef](#)]
43. Li, Q.; Li, L.; Zheng, L.; Liu, E.; Guo, J.; Shanglin, Y. Non-equilibrium grain boundary segregation kinetics of phosphorus in 12Cr1MoV steel at different solution temperatures. *J. Mater. Sci.* **2004**, *39*, 6551–6554.
44. Salje, G.; Feller-Kniepmeier, M. The diffusion and solubility of copper in iron. *J. Appl. Phys.* **1977**, *48*, 1833–1839. [[CrossRef](#)]
45. Babapour, A.; Hosseinipour, S.J.; Jamaati, R.; Abbasi, M. Effect of Sb and Initial Annealing on the Microstructure, Texture, and Magnetic Behavior of Low Silicon Steel Produced by Single-Roll Drive Rolling. *Met. Mater. Int.* **2022**, *29*, 1815–1824. [[CrossRef](#)]
46. Chen, C.; Zhou, J.; Yu, J.; Ju, J.; Zhang, Y.; Wang, J.; Fan, B. Interfacial microstructures and infiltrated cracks in tin bronze/steel bimetallic materials fabricated by arc cladding. *J. Mater. Sci.* **2023**, *58*, 4679–4693. [[CrossRef](#)]

Disclaimer/Publisher’s Note: The statements, opinions and data contained in all publications are solely those of the individual author(s) and contributor(s) and not of MDPI and/or the editor(s). MDPI and/or the editor(s) disclaim responsibility for any injury to people or property resulting from any ideas, methods, instructions or products referred to in the content.